Exploring Reaction Pathways of Single-Molecule Interactions through the Manipulation and Tracking of a Potential-Confined Microsphere in Three Dimensions

Wesley P. Wong[1,3], Volkmar Heinrich[1], and Evan Evans[1,2]

[1]Department of Biomedical Engineering, Boston University, Boston, MA 02215, USA.
[2]Department of Physics, Boston University, Boston, MA 02215, USA.
[3]Department of Physics, Harvard University, Cambridge, MA 02138, USA.

ABSTRACT

Weak non-covalent interactions between single molecules govern many aspects of microscopic biological structure and function, e.g. cell adhesion, protein folding, molecular motors and mechanical enzymes. The dynamics of a weak biomolecular bond are suitably characterized by the kinetic transport of molecular states over an effective energy landscape defined along one or more optimal reaction pathways. Motivated by earlier developments [1,2], we present a novel method to quantify subtle features of weak chemical transitions by analyzing the 3D Brownian fluctuations of a functionalized microsphere held near a reactive substrate. A weak optical-trapping potential is used to confine motion of the bead to a nanoscale domain, and to apply a controlled bias field to the interaction. Stochastic interruptions in the monitored bead dynamics report formation and release of single molecular bonds. In addition, variations in the motion of a bead linked to the substrate via a biomolecule (a protein or nucleic acid) signal conformational changes in the molecule, such as the folding/unfolding of protein domains or the unzipping of DNA. Thus, energy landscapes of complex biomolecular interactions are mapped by identifying distinct fluctuation regimes in the 3D motion of a test microsphere, and by quantifying the rates of transition between these regimes as mediated by the applied confining potential.

The 3D motion of the bead is tracked using a reflection interference technique combined with high-speed video microscopy. The position of the bead is measured over 100 times per second with a lateral resolution of ~3-5 nm and a vertical resolution of ~1-2 nm. Crucial to the interpretation of results, a Brownian Dynamics simulation has been developed to relate the statistics of bead displacements to molecular-scale kinetics of chemical interactions and structural transitions. The experimental approach is designed to enlarge the scope of current techniques (e.g. dynamic force spectroscopy [3]) to encompass near-equilibrium forward/reverse transitions of weak-complex interactions with multiple binding configurations and more than one transition pathway.

INTRODUCTION

"Weak" biomolecular bonds are characterized by much smaller binding energies than covalent bonds, and typically are on the order of 10-30 k_BT in thermal energy units (here k_B is the Boltzmann constant, and T ~300 K is temperature, i.e. $k_BT \approx 4\times10^{-21}$ J). Therefore, in the aqueous environment of the cell, thermal activation alone is capable of disrupting a weak bond, which leads to characteristic bond lifetimes ranging from microseconds to a year. Biological molecules involved in complex interactions like protein folding or bioreceptor-ligand chemistry are themselves extremely complicated mesoscopic systems, each composed of thousands to

millions of atoms. Yet most methods in solution biochemistry, as well as many force-probe studies of single-biomolecule interactions are viewed in the context of a standard paradigm, in which the dynamics of bonds or changes in conformations are described in terms of forward and reverse reaction rates between two distinct chemical states with different energies and separated by an intervening barrier. The impact of pulling on a bond or structure with a force probe is idealized by addition of a linear mechanical potential to a free energy contour assumed to regulate kinetic transport between the two states. In the most simple case (described below), this biochemical paradigm implies an exponential dependence of the kinetic rates on force, which has been used with great success to model the outcome of many single-molecule tests, studying e.g. the strengths of bioadhesion bonds, unfolding of protein domains, intramolecular transitions in polysaccharide chains, slowing molecular motors, etc. [3]. However, we now realize that the present state-of-the art probe methods provide only "snapshots" of a more complex (and important) behavior, which has remained hidden because of the limited dynamic range and the select history or protocol of force application. To fully explore such complex behavior and obtain a more fundamental understanding of nature's design in nanoscale biology, new approaches and instruments are needed to reveal the subtle dynamics of single-molecular interactions.

Conventional mode of force spectroscopy and emerging challenges

The development of dynamic force spectroscopy (DFS) has given us a useful framework for guiding our thinking about how to test single-molecule transitions with external fields [3-5]. The crucial concept is that force-mediated transitions in weakly interacting systems do not occur at a single characteristic value of the applied force. Instead, thermal activation inextricably couples force to time. In the most simple physics, transitions on laboratory time scales are modeled by kinetic-diffusive transport of molecular states over an *energy landscape*. This landscape represents the potential of mean force along a reaction coordinate (i.e. a *free* energy contour excluding the displacement degree of freedom), leading from a bound minimum—passing over one or more intervening barriers—to an unbound state at higher energy. A one-dimensional example of an energy landscape mapped along a particular reaction pathway is sketched in Figure 1.

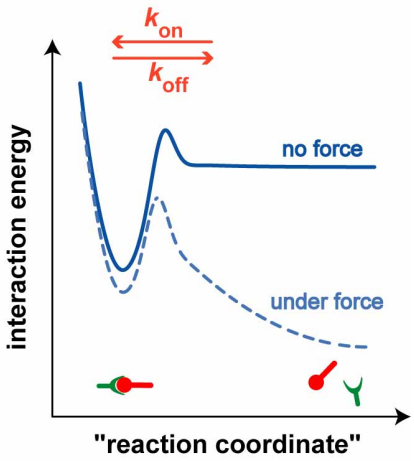

Figure 1. Schematic energy landscape governing the interaction of two biomolecules *(solid line)*; and the impact of a mechanical potential contributed by pulling with a force probe *(dashed line)*.

Application of force adds a mechanical potential proportional to the projection of the force along the spatial pathway, which tilts the landscape, and thereby lowers, shifts, and narrows the energy barrier [4]. Due to the drop of the energy barrier, application of a mechanical field dramatically increases the rate k_{off} of the forward transition, while quenching the reverse rate k_{on}. In the simplest case where a sharp barrier confines narrowly bound states, the barrier energy falls linearly with increasing probe force f, causing the forward-transition rate to grow exponentially [$k_{off} \approx k_{off}^{o} \exp(f/f_{\beta})$] while k_{on} quickly vanishes (k_{off}^{o} is the unstressed off rate). As first postulated by Bell [6], the thermal force scale $f_{\beta} = k_B T/x_{ts}$ for rate exponentiation is set by the average projected location x_{ts} of the energy barrier along the

reaction coordinate selected by force. Moreover, it is easily shown that pulling apart such an *ideal* bond with a steady ramp of force in time yields a *universal* distribution of rupture forces [4] where the distribution peak—i.e. the most frequent transition force f^*—shifts upward in direct proportion to the logarithm of the loading speed $r_f = df/dt$, i.e.

$$f^* = f_\beta \log[r_f/(k_{off}^o f_\beta)]$$

As a mechanical corollary to the standard paradigm of solution biochemistry, this relation has been the hallmark of DFS applications in many single-molecule force experiments [3,5]. An illustration of seemingly ideal bond fracture is shown by measurements of the most frequent force needed to rupture the bioadhesion complex PSGL-1:P-selectin, plotted in Figure 2a as a logarithmic function of the loading speed [7]. Tested under steady ramp conditions, the linear shift in the most likely breaking force with log(loading rate) was well defined between 300 and 30,000 pN/s (*large solid red triangles*), which showed that two parameters governed mechanical strength in this regime: $k_{off}^o = 0.35$/s, and $f_\beta = 18$ pN, implying $x_{ts} = 0.22$ nm (!). As such, the dynamic force spectrum provided a clear image of a prominent barrier along the direction of force.

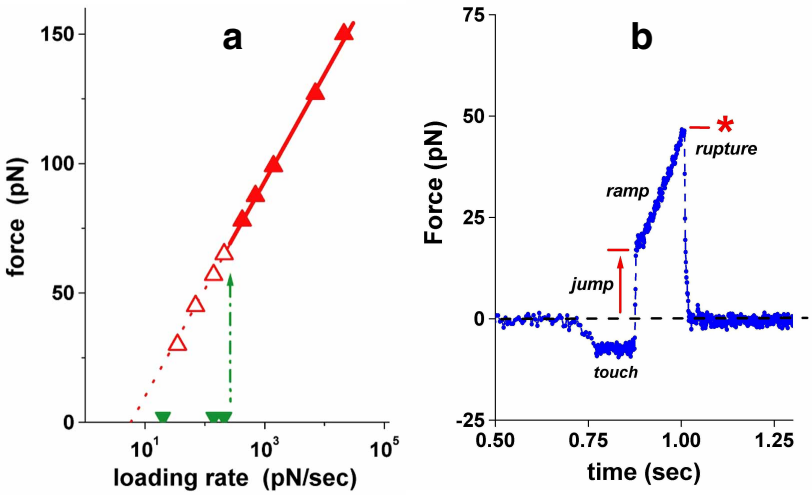

Figure 2a. Dynamic force spectrum for detachment of the endothelial cell adhesion molecule P-selectin from the leukocyte glycoprotein ligand PSGL-1 (measured with a biomembrane force probe [7]). Under steady force ramps, a first-order dynamical transition occurs in strength (solid red/green triangles) as the consequence of two kinetic pathways for bond dissociation. **2b.** Detachment of a PSGL-1:P-selectin bond under a jump/ramp mode, which eliminated one pathway but not the other (open red triangles).

However, the successful imaging of one prominent kinetic barrier by DFS can be misleading when complex interactions are only examined in a limited window of loading rates and strictly in the conventional "steady ramp" mode. For instance, it was initially puzzling that the most frequent rupture force for PSGL-1:P-selectin bonds shifted precipitously to near zero under steady loading rates below 300 pN/sec (*bottom solid green wedges* in Figure 2a). But when tested with a new DFS *jump/ramp* protocol (cf. Figure 2b), the force-distribution peak for PSGL-1:P-selectin rupture events reappeared at higher forces and continued the upper branch of the spectrum down to slow loading speeds (*open red triangles*). In this way, the PSGL-1:P-selectin interaction was shown to behave as a mechano-chemical switch, with force selecting between two thermodynamic pathways for dissociation [7]. Thus, it has become clear that the emerging challenge is to design force instruments that will bridge the gap between near-equilibrium transitions on long time scales (often with multiple pathways as is demonstrated by PSGL-1:P-selectin) and the far-from-equilibrium transitions on fast time scales already assessable by conventional DFS techniques.

Exploring the Crossover between Near-Equilibrium and Far-from-Equilibrium Transitions

Here, we describe a novel approach that extends traditional single-molecule force spectroscopy to include the nanoscale dynamics of bidirectional transitions. Building on earlier concepts [1,2], the underlying idea is simple: that the characteristic footprint of near-equilibrium phenomena can be encoded in the three-dimensional Brownian fluctuations of a functionalized glass bead confined near a reactive substrate by a weak external potential.

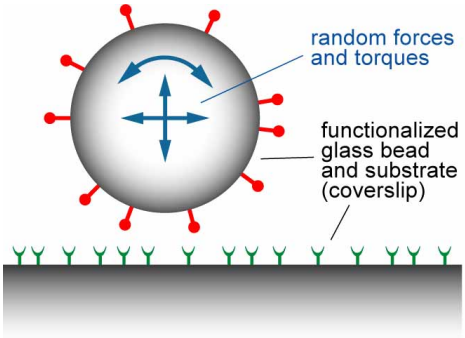

Figure 3. Sketch of a functionalized glass bead suspended near a reactive substrate (microscope coverslip). Random forces and torques imparted by the aqueous environment cause the bead to undergo Brownian motion. Red and green symbols represent, for example, complementary bioadhesion molecules.

As illustrated schematically in Figure 3, a small (1-2 μm in radius) glass microsphere is suspended in an aqueous buffer and held near a glass coverslip. The bead is functionalized with a biological molecule, such as a receptor protein, and the coverslip is coated with the reactive counterpart or specific ligand. In the thermalized, aqueous environment, the bead undergoes overdamped Brownian motion, performing a random walk above the substrate. However, when a bond forms between a molecule on the sphere and one on the coverslip, the bead motion is altered dramatically by its tether to the surface. As a consequence, the bead exhibits constrained fluctuations in position, generally distributed over a spherical cap. If a second bond forms before the first bond breaks, motions of the twice-tethered bead are now distributed along a curved arc. Thus, by quantifying the free or constrained nanoscale fluctuations in position of the bead, we are able to discriminate between the formation and release of single molecular bonds. Similarly, tracking the detailed displacements of a bead can reveal unfolding/refolding of domains within a protein that links the sphere to the substrate.

The crucial requirement is to design an instrument that will provide nanoscale resolution of the 3D bead position on fast to long time scales (milliseconds to minutes). Moreover, in order to explore near-equilibrium transitions with barrier crossings in both directions, the molecular events have to be localized to a small but defined reaction volume by adding a very weak bias potential to the energy landscape. To fulfill this requirement, we have combined a high-numerical-aperture optical trap with high-resolution, optical interference microscopy, and fast video image processing. In the next two sections, we present this apparatus in detail, as well as preliminary results. This is followed by an outline of a Brownian Dynamics simulation that we have developed to extract the kinetics of chemical transitions from measurements of bead dynamics.

EXPERIMENTAL DESIGN AND OPERATION

3D Bead Tracking

To track the position of the bead in three dimensions we use Reflection Interference Contrast Microscopy (RICM) combined with high-speed video microscopy. The bead is illuminated through the objective of an inverted optical microscope and imaged with reflected light as shown in Figure 4. Part of the reflected light originates from the cover glass/water

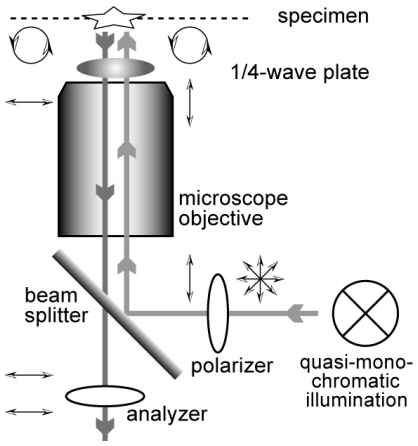

Figure 4. Schematic overview of the main microscope components used for RICM. Incident light is generated by a 100W Hg arc lamp, passed through an interference filter (546 ± 5nm, not shown), and focused in the objective's back-focal plane to give Köhler epi-illumination. The illuminating numerical aperture can be adjusted with an iris placed conjugate to the back-focal plane (not shown). A polarizer / ¼-wave plate / analyzer assembly minimizes internal reflections.

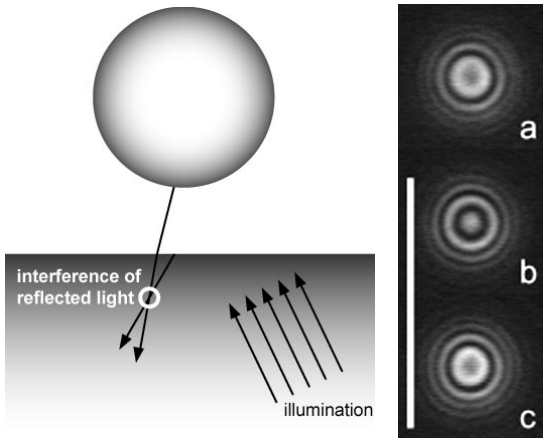

Figure 5. ***Left:*** Interference generated by light components reflected back from the coverslip/ buffer interface and from the underside of the glass microsphere.
Right: Series of RICM fringe patterns of a glass sphere at different gap heights h above the coverslip: 230nm (a), 130nm (b), and 30nm (c). The white bar corresponds to 10μm.

interface, another part is back-scattered from the underside of the bead. The light reflected from these two surfaces interferes to form a Newton-ring pattern as shown in Figure 5. This image pattern is digitized by a high-speed video camera and then analyzed with custom-written software to determine the 3D position of the bead as well as its radius. The center of the pattern reveals the lateral position of the bead, whereas the concentric fringes encode the bead height above the coverslip.

High-speed *lateral* tracking of the bead position is achieved through a sequence of algorithms that increasingly refine the position of the circularly symmetric pattern: *(i)* weighted center-finding of intersecting intensity gradients; *(ii)* normalized cross-correlation of the pattern with horizontally or vertically flipped mirror images of itself; and *(iii)* non-linear fit to a symmetric model function with adjustable center. Once the bead center is known, the circularly averaged radial intensity profile is computed and analyzed to determine the bead height and radius (see below). The resolution of this method is ~3-5 nm in the lateral dimension and ~1-2 nm in the vertical dimension. With our current video camera we are able to determine the bead position over 100 times per second. Faster video cameras with kHz frame rates can be used to further increase the time resolution of this technique.

We focus the microscope objective at the plane of the coverslip/water interface. Therefore, the interference pattern formed in this plane dominates the intensity distribution picked up by our high-NA (1.25) oil-immersion objective. Circularly averaged to improve the signal-to-noise ratio, the radial intensity profile obtained from this pattern is correlated with a model that predicts the profile as a function of gap height and bead radius. This model is

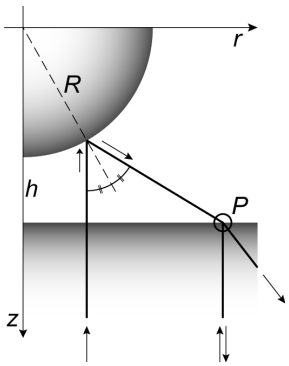

Figure 6. Self-interference of the reflected components of an illuminating, on-axis plane wave. The sketch illustrates the geometry used to calculate the optical path difference of the two rays interfering at point P in the coverslip/buffer interface. The directions of ray propagation are indicated by small arrows.

based on a simplified ray-optics description, and it approximates the angular illumination spectrum with a single, on-axis plane wave (cf. Figure 6). Taking advantage of a strict focus protocol [8], we use the following semi-empirical expression [9] to analyze the radial intensity profile:

$$I(r) = A_0 + A_1 \exp\left(-b_1 r^2\right) + A_2 \exp\left(-b_2 r^2\right) \cos \Delta\Phi(r).$$

In this formula, r represents the distance from the center of the pattern, $\Delta\Phi(r)$ the phase difference between the light reflected from the coverslip/water interface and the light reflected from the bead at a given r, and $\{A_0, A_1, A_2, b_1, b_2\}$ a set of empirical fitting parameters. The phase difference is given by

$$\Delta\Phi(r) = \frac{2\pi\Lambda(r)}{\lambda_0} + \pi$$

where $\Lambda(r)$ is the optical path difference, and λ_0 is the wavelength of the interfering light in vacuum. A constant phase shift of π is contributed by reflection at the higher-index glass bead. Approximating the underside of the bead as a paraboloid, the following expression for $\Lambda(r)$ is obtained:

$$\Lambda(r) = \frac{1}{2} n_{\mathrm{H_2O}} \left[2h - R + \sqrt{4r^2 + (2h+R)^2} \right]$$

where R is the bead radius, h is the gap height between the bead and the coverslip (cf. Figure 6), and $n_{\mathrm{H_2O}}$ is the index of refraction of water.

Considering the approximations used in this model, as well as the complexity of the overall imaging system, it is crucial to test this model carefully. A typical non-linear fit of the radial intensity formula to actual bead data is presented in Figure 7, demonstrating good agreement between the measured and predicted pattern at a given height. However, as an ultimate test of the validity of the model one should also verify its ability to reproduce known

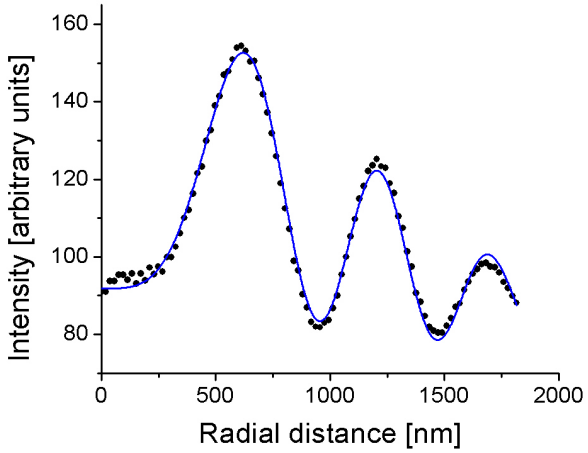

Figure 7. Nonlinear fit *(solid line)* of our model to a radial intensity profile. The symbols represent circularly averaged intensities obtained for half-pixel (~19nm) wide radial bins. The overall range of the shown intensity profile is roughly the same as the bead radius, measured to be 1816 nm.

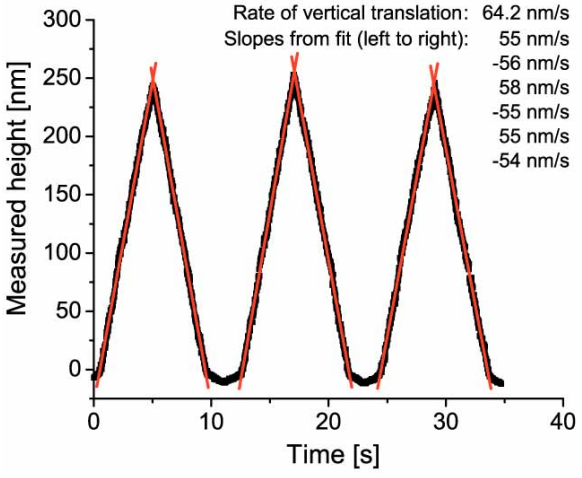

Figure 8. Bead height h measured by RICM during piecewise linear, triangular vertical translation of a pipette-aspirated bead. A closed-loop piezo actuator provided sub-nanometer translation resolution. The measured slopes allow us to verify our theoretical distance prediction over a large range of heights and, if necessary, to calibrate the model.

height *changes* of a given bead. To do so, we hold the bead in a vertically mounted micropipette that can be moved up and down with sub-nanometer accuracy using a closed-loop piezo actuator. Figure 8 shows the measured bead height for a piezo-driven, triangular vertical displacement of a ~5μm (diameter) bead. The data correctly reproduces the linearity of bead motion over the whole range of ~300 nanometers. The bottom of the triangular waveform is blunted as the bead was pressed against the coverslip here. A straight line is fit to the data of each linear segment to determine the vertical bead velocity. The measured slopes are reasonably consistent with each other, varying less than 5% from the average slope of 55.5 nm/s. A systematic error of ~14% is noticed between the average slope and the set velocity; however, once determined by a pre-calibration run, this error can easily be corrected for in recorded raw height data.

When evaluating the resolution of the vertical position detection, we must also take into account the level of system noise, which is estimated by the ~1 nm standard deviation in the measured heights of surface-*immobilized* beads. Thus, when examining relative bead-height changes over a range of ~20 nm for a calibrated system, the measurement error is ~1-2 nm. Note that the systematic error can be reduced by decreasing the maximum angle of the illuminating light. Although the resulting lower light level also decreases the signal-to-noise ratio, this approach is useful in situations where height calibration is not possible. We anticipate further improvement of pattern prediction by including additional features of the optical system in the model presented above.

Bead Confinement

Crucial for near-equilibrium DFS studies, our system is equipped with a laser-optical trap to confine the bead in a weak potential, and to apply controlled stresses to linkages between the bead and the substrate [10]. The single-beam gradient trap is generated by a 4 W, 1064 nm Nd:YAG diode laser that is focused (by the microscope objective) slightly above the coverslip. A piezo-controlled beam colliminator allows us to move the center of the laser trap up and down along the optical axis. The trapping power can be varied quickly and accurately with a liquid-crystal power controller.

PRELIMINARY RESULTS

Free Bead

We first tested our 3D RICM tracking system by recording the positions of non-reactive beads near a BSA covered surface. Figure 9 shows the lateral trajectory of a typical unattached bead. Histograms of changes in bead position (along the *x*-axis) during a specified time interval are shown in the left panel of Figure 10 for three different, increasing time steps Δt. For unimpeded Brownian motion, the variances of these distributions are expected to grow linearly in time, with a proportionality constant of $2D$ (D denoting the diffusion constant). The mean square displacements parallel to the coverslip are plotted as a function of Δt in Figure 10 (right panel). For two-dimensional diffusion, the slope of a linear fit to

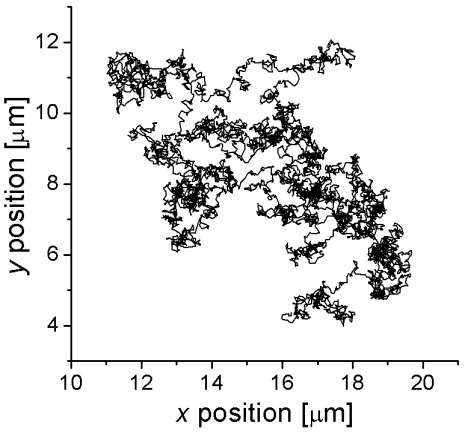

Figure 9. Two-dimensional projection of the random walk of a ~3μm (diameter) bead whose position was recorded every ~40ms.

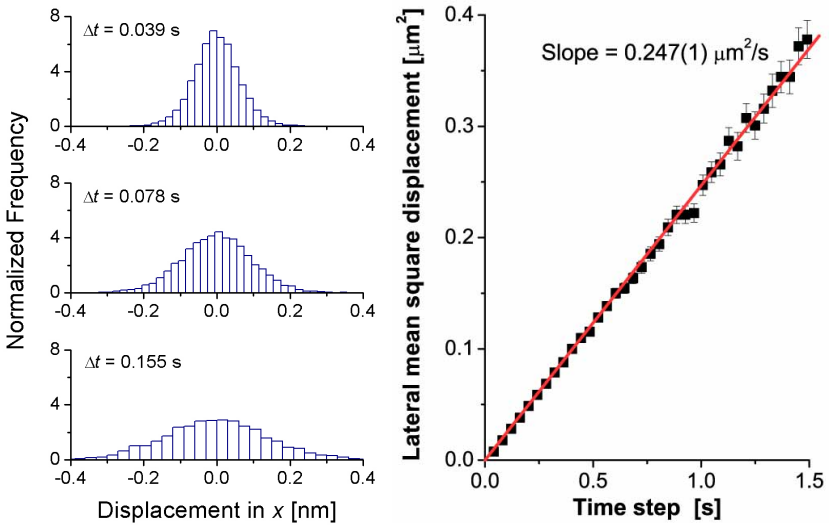

Figure 10. ***Left:*** Histograms of one-dimensional bead displacements obtained for the random walk of Fig. 9 at increasing time steps Δt. The growing spread of the distributions is consistent with free Brownian motion of the bead. ***Right:*** 2D mean square displacements $\langle \Delta x^2 + \Delta y^2 \rangle$ as a function of the time interval Δt for the same data set. As expected for unimpeded, drift-free diffusion, the relationship is linear. The slope of the linear fit equals four times the effective, near-wall diffusion coefficient for the bead's lateral motion at the given range of bead heights (cf. Figure 11).

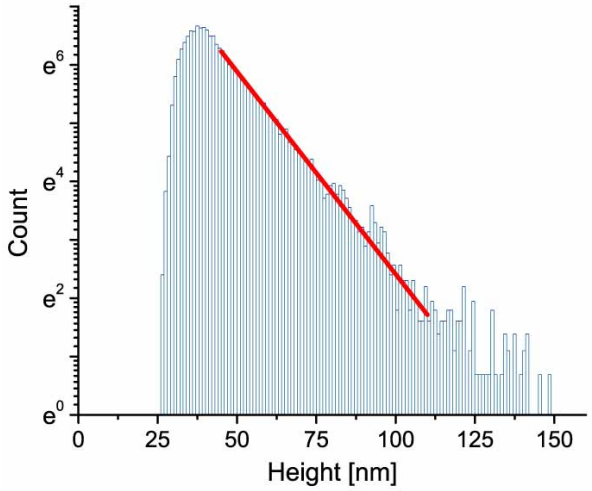

Figure 11. The histogram of bead heights h measured by RICM for the random walk of Figure 9 images the (negative) free energy of the bead. The non-zero minimum bead height and part of the steric repulsion at low distances are due to the presence of adsorbed BSA layers. Beyond the most frequent height of ~40nm, the free energy is clearly dominated by the linear gravitational potential of the bead.

the data is divided by four to give an effective diffusion coefficient for lateral motion of $D_{xy} = 0.0618(3)\ \mu m^2/s$.

The distribution of heights along this trajectory is presented in the semi-logarithmic plot of Figure 11. For a system in thermodynamic equilibrium at temperature T, the probability that the system is in state x is proportional to the Boltzmann weight, $\exp[-G(x)/k_B T]$, where $G(x)$ is the free energy of the system. Therefore, this histogram directly images the free energy of the bead as a function of bead height. For bead-to-wall distances between 45 nm and ~110 nm, the figure clearly reveals a linear energy potential. Interpreting this linear potential as gravity, we can use the depicted slope to *weigh* our bead fairly accurately! Using a density of 2.50 g/cm³ for the borosilicate bead, we obtain its radius from the bead weight as 1.67 μm—very close to the value of 1.63 μm determined via RICM.

Trapped Bead

To determine the three-dimensional confinement potential as a function of laser power, we have monitored the constrained Brownian motion of trapped beads at varying settings of the laser power controller. Example bead positions are presented in Figure 12. As demonstrated above for the heights of a free bead, the statistics of bead positions reflect the free energy of the system. For the x-z-data shown in the left column of Figure 12 (z denotes the vertical direction, cf. Figure 6), this energy encompasses gravity, buoyancy, the optical trapping

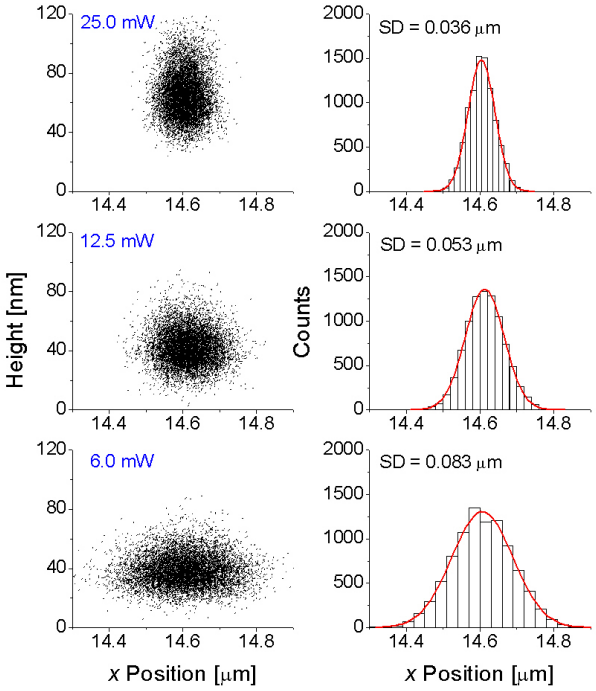

Figure 12. 3D-confinement potential of the optical trap at different laser powers. ***Left:*** The measured positions of the bead's lowest point were projected onto the *x*-*z*-plane to illustrate the "energy cocoon" created by the laser trap. ***Right:*** Gaussian distributions of the bead's *x*-positions reveal a harmonic *lateral* trapping potential.

potential, and the energy contributions of bead-substrate interactions. On the other hand, the change in free energy in *lateral* directions arises primarily from the optical potential of the laser trap. Well-described as Gaussian, the distributions of *x*-positions of the bead measured at three different laser powers and shown in the right column of Figure 12 imply that the lateral trapping well is harmonic. The variance of each distribution allows us to calculate the effective lateral spring constant of the optical trap at the given (set) laser power; in this example it ranges from ~0.6 pN/µm at 6 mW to ~3 pN/µm at 25 mW.

Tethered Bead

Let us next examine a bead that was attached to the surface. Attachment is evident not only in the constricted lateral bead motion, but also in the reduced fluctuations in height. This is illustrated in Figure 13, which compares height fluctuations of a free bead with those of a bead that adhered to the BSA layer. Figure 14 shows the fluctuations of the tethered bead in more detail and over a longer period of time. A noticeable further reduction in height fluctuations is seen between the times labeled t_A and t_B —obviously corresponding to a temporary *multiple* attachment of the bead to the bottom surface.

Figure 15 provides for an even more detailed inspection of the recorded 3D bead

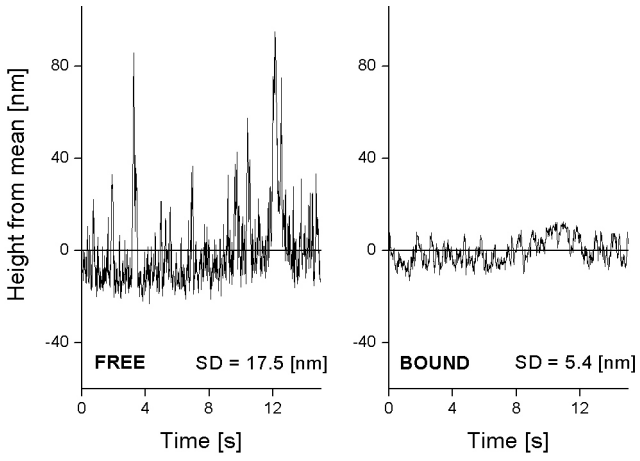

Figure 13. Height fluctuations of a free bead *(left)* and of a bead that was tethered to the surface *(right)*.

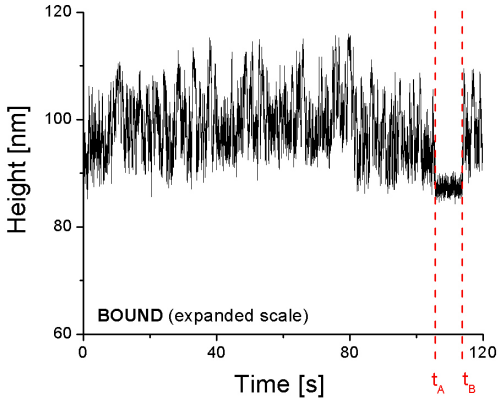

Figure 14. Extended tracking of the tethered bead from the right panel of Figure 13 revealed a time interval (t_A,t_B) with dramatically reduced height fluctuations—which is best interpreted as the signature of a temporary multiple attachment.

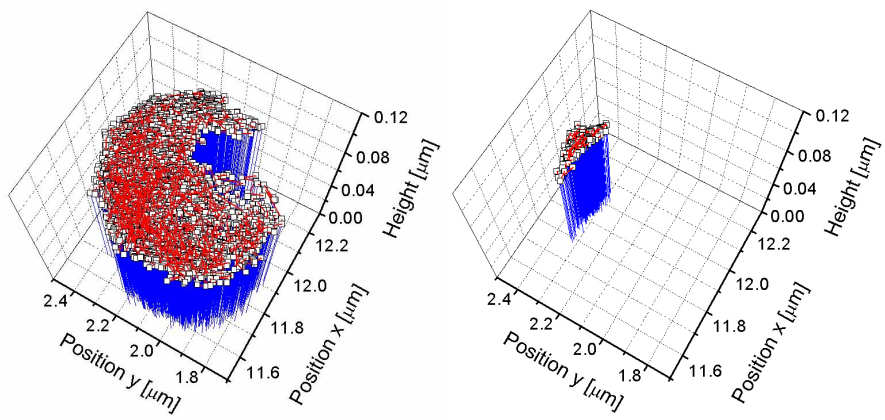

Figure 15. 3D plots of the positions of the tethered bead of Figure 14. ***Left:*** Roughly distributed about a spherical cap, the positional data imply that a single tether linked the bead to the substrate. ***Right:*** Fluctuations in the time interval (t_A,t_B) (cf. Figure 14) are distributed about a short arc—consistent with two distinct linkers between bead and substrate.

positions, leading to the conclusion that this multiple attachment is most likely a double linkage between the bead and the substrate. The bead positions in the first plot (Figure 15, left) are distributed about a spherical cap, consistent with the expected motion of a bead anchored to the surface by a single tether (with some repulsion from the surface). The second 3D plot (Figure 15, right) shows the trajectory within the smaller time interval from t_A to t_B. Here, the motion of the bead is more or less constrained along a curved line, implying two attachments to the surface.

BROWNIAN DYNAMICS SIMULATION

To deduce single-molecule kinetics from careful analysis of bead-motion data, a detailed understanding of the dynamics of this system is essential. Thus, we have a developed a multi-scale Brownian Dynamics simulation of a functionalized bead suspended in water near a reactive substrate. The model takes into account the detailed hydrodynamics of a spherical particle near a wall as well as microscopic elements of molecular structure and chemical interaction.

The stochastic bead displacements relative to the substrate are described by a Brownian Dynamics algorithm that includes the relevant hydrodynamics effects, such as the coupling of translational and rotational modes due to the proximity of a wall [11]. The change in bead configuration within a discrete time step is based on an integration of the Langevin equation at low Reynolds numbers [12]. Thus, inertial effects are neglected, and the water surrounding the bead is treated as a continuous medium. The water interacts with the bead via a drag force (or torque) that is proportional to the velocity (or angular velocity) of the bead, as well as by imparting random thermal kicks that cause the bead to undergo Brownian motion. Specifically, the change in the i-th component of position/orientation during a time step Δt is given by the formula

$$\Delta r_i = \sum_j \frac{D_{ij} F_j}{k_B T} \Delta t + \sum_j \frac{\partial D_{ij}}{\partial r_j} \Delta t + R_i(\Delta t) \, .$$

D_{ij} is the 6x6 diffusion matrix, F_j is the generalized force consisting of 3 components of force and 3 components of torque, and $R_i(\Delta t)$ is a random displacement chosen from a Gaussian distribution such that $\langle R_i(\Delta t)\, R_j(\Delta t) \rangle = 2D_{ij}\Delta t$. The matrix $\boldsymbol{D}$ is related to the grand mobility matrix $\boldsymbol{M}$ by the Einstein equation, $\boldsymbol{D}/k_BT = \boldsymbol{M}$. $\boldsymbol{M}$ is the inverse of the multidimensional friction coefficient, i.e., of the matrix of proportionality constants between drag force and velocity components. The mobility matrix $\boldsymbol{M}$ can be computed from the Navier-Stokes

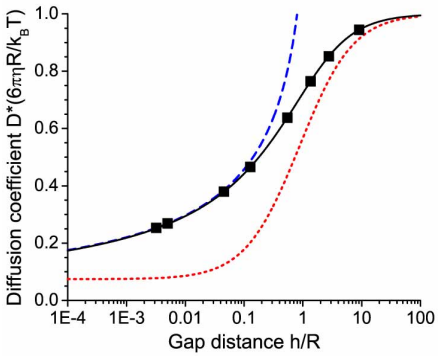

Figure 16. Dimensionless lateral diffusion coefficient for motion of a sphere of radius R at a distance h from a wall in a fluid with viscosity η. The graph compares exact numerical solutions (*symbols* [14]) with asymptotic formulae (*dashed line* and *dotted line* [14]) and with the approximation (*solid line* [13]) that is used by our simulation.

equations of fluid dynamics. For a sphere near a wall, it is a height-dependent 6x6 matrix that couples rotations and translations of the bead. Our simulation uses the analytic approximation developed by Perkins and Jones [13] that agrees well with the classic asymptotic formulae in their respective regimes, and that lies within 1% of all calculated, exact numerical results [14]. The predicted height dependence of the diffusion coefficient for motion parallel to the plane is presented in Figure 16.

In our model, forces on the bead include the ever-present non-specific interactions between bead and substrate described by the classical DLVO theory (screened electrostatic repulsion and van der Waals attraction [15]), plus a steric repulsion arising from the polymers at the surface. Added to this is the gravitational force acting on the bead, and the optical forces due to the single-beam gradient laser trap. These forces can be chosen to match the experimental free-energy profile of the bead as measured by the statistics of bead position.

To incorporate specific chemical interactions, we take advantage of the large separation in time scales between the dynamics of receptor/ligand groups and the motion of the bead. In our multi-scale approach, the position of each reactive molecular site is coarse-grained and described by an effective probability density. As the active sites are attached to the surface by polymer linkers, the shape of this probability distribution is assumed to be hemispherical (cf. Figure 17). These active sites are placed randomly on the surface at a density chosen to match the experimental conditions.

Whenever the probability domes of two complementary molecules overlap, the simulation creates a bond with a probability that is proportional to the joint probability density integrated over the volume of overlap. The proportionality constant is the length of the discrete time step multiplied by an effective on rate for this nanoscale reaction volume. For a simple model that assumes a constant probability density within each hemisphere, the probability of forming a bond between two reactive molecules during an infinitesimal time interval δt is

$$P(\delta t) = k_{on}[A][B]V_{\text{overlap}}\delta t$$

where k_{on} is the effective on rate, $[A]$ and $[B]$ are effective concentrations of the two reactive species within the hemispheres (equal to 1/volume of the hemisphere in this simplified case), and V_{overlap} is the overlap volume of the two probability domes. For finite time steps Δt, this formula extrapolates to

$$P(\Delta t) = 1 - \exp(-k_{on}[A][B]V_{\text{overlap}}\Delta t)$$

provided that a bond that forms within this time does not break before the end of the time interval.

Bond breakage is simulated by a model of the force-dependent off rate, taking into account the instantaneous stresses exerted by the bead dynamics. For a simple barrier,

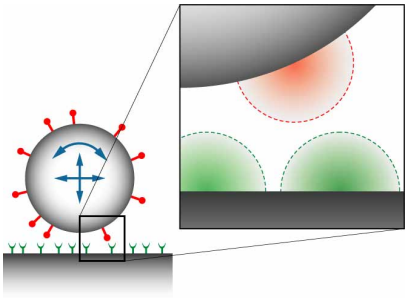

Figure 17. Illustration of the coarse-graining of reactive sites in the multi-scale Brownian Dynamics simulation. Surface-linked test molecules are described by hemispherical probability domes (*inset*).

for example, the probability of bond failure per unit time is modeled by a characteristic off rate multiplied by the exponential of the change in barrier height due to force.

CONCLUSIONS

We have described a novel apparatus and method for analysis of single-bond dynamics by tracking Brownian fluctuations of a functionalized bead. Our preliminary tests have shown that bonding events between molecules immobilized on the bead and on the substrate can be detected with clear discrimination of single-molecule attachments, and that nanoscale bead-tethering dynamics are accurately reported. As the next step defining the "proof of principle", we are currently preparing experiments to examine interactions between and within biomolecules, concentrating on molecules for which we have already identified multiple binding configurations and transition pathways. Under soft confinement by the optical trapping potential, we expect the microsphere dynamics to distinguish multiple bonding distances, and more significantly, to reveal major changes in the duration of fluctuation regimes as a consequence of the exploration of nearby metastable states separated only by small energy barriers.

ACKNOWLEDGEMENT

This work was supported by USPHS grant HL65333 from the National Institutes of Health.

REFERENCES

1. E.-L. Florin, A. Pralle, E. H. K. Stelzer, and J. K. H. Hörber, *Appl. Phys. A* **66**, S75-S78 (1998).
2. A. Rohrbach, E. Florin, and E. H. K. Stelzer, *Proc. SPIE* **4431**, 75-86 (2001).
3. E. Evans, *Ann. Rev. Biophys. & Biomol. Structure* **30**, 105-128 (2001).
4. E. Evans and K. Ritchie, *Biophys. J.* **72**, 1541-1555 (1997).
5. E. Evans, and P. Williams, in *Physics of Bio-Molecules and Cells, Ecoles des HOUCHES d'Ete LXXV*. (EDP Sciences - Springer-Verlag, 2002) pp. 145-185; P. Williams and E. Evans, *ibid*, pp. 186-203.
6. G. I. Bell, *Science* **200**, 618-627 (1978).
7. E. Evans, V. Heinrich, A. Leung, and C. Zhu (in preparation)
8. V. Heinrich, K. Ritchie, N. Mohandas, and E. Evans, *Biophys. J.* **81**, 1452-1463 (2001).
9. J. Rädler and E. Sackmann, *Langmuir* **8**, 848-853 (1992).
10. M. P. Sheetz (editor), *Laser tweezers in cell biology. Volume 55 of Methods in Cell Biology* (Academic Press, 1998).
11. D. L. Ermak and J. A. McCammon, *J. Chem. Phys.* **69** (4), 1352-1360 (1978).
12. M. Doi and S. F. Edwards, *The Theory of Polymer Dynamics* (Clarendon Press, Oxford, 1986) pp. 46-90.
13. G. S. Perkins and R. B. Jones, *Physica A* **1889**, 447-477 (1992).
14. A. J. Goldman, R. G. Cox, and H. Brenner, *Chem. Eng. Sci.* **22**, 637-651 (1967).
15. J. I. Israelachvili, *Intermolecular and Surface Forces*, 2nd ed. (Academic Press, New York, 1991) pp. 450.